Semiclassical deconstruction of quantum states in graphene

Douglas J. Mason,[1] Mario F. Borunda,[1,2] and Eric J. Heller[1,3]

[1]*Department of Physics, Harvard University, Cambridge, Massachusetts 02138, USA*
[2]*Department of Physics, Oklahoma State University, Stillwater, Oklahoma 74078, USA*
[3]*Department of Chemistry and Chemical Biology, Harvard University, Cambridge, Massachusetts 02138, USA*

We present a method for bridging the gap between the Dirac effective field theory and atomistic simulations in graphene based on the Husimi projection, allowing us to depict phenomena in graphene at arbitrary scales. This technique takes the atomistic wave function as an input, and produces semiclassical pictures of quasiparticles in the two Dirac valleys. We use the Husimi technique to produce maps of the scattering behavior of boundaries, giving insight into the properties of wave functions at energies both close to and far from the Dirac point. Boundary conditions play a significant role to the rise of Fano resonances, which we examine using the processed Husimi map to deepen our understanding of bond currents near resonance.

I. INTRODUCTION

With interest and experimental capabilities in graphene devices growing,[1–8] the need has never been greater to improve our understanding of quantum states in this material. Despite the success of the Dirac effective field theory for graphene,[9] however, many technological proposals arise from predictions using the more fundamental tight-binding approximation.[10–13] This is because the atomistic model that underlies the Dirac theory is able to incorporate phenomena such as scattering from small defects,[14–18] ripples,[19] or edge types[20–22]—all of which promise technological applications. However, atomistic calculations are computationally expensive, and replacing these features with scattering theories in a more efficient Dirac model introduces substantial challenges. A robust approach that can analyze the atomistic wave function to produce semiclassical pictures of quasiparticles in the two Dirac valleys remains to be seen.

To address these issues and expand our understanding of graphene quantum states, we use the processed Husimi projection technique, introduced by Mason *et al.*,[23–25] to produce snapshots of the local momentum distribution and underlying semiclassical structure in graphene wave functions. When processed Husimi projections are calculated at many points across a system, the processed Husimi map that results provides a semiclassical picture of the atomistic wave function. In this article, we define the processed Husimi map for graphene systems (Sec. II), and use it to deepen our understanding of boundary conditions in both high-energy relativistic scar states[26,27] (Sec. III A), and states near the Dirac point (Sec. III B). We then use the processed Husimi maps and Husimi flux map semiclassical techniques to interpret Fano resonances[28–30] within this novel material (Sec. III C).

II. METHOD

A. Definition of the Husimi projection

The conduction band of the graphene system can be approximated as a honeycomb lattice with a single p_z orbital located at each carbon-atom lattice site.[9] The Husimi function is defined as the coherent state projection of a wave function $\psi(\{\mathbf{r}_i\})$ defined at each orbital, where the coherent state

$|\mathbf{r}_0,\mathbf{k}_0,\sigma\rangle$ describes an envelope function over those sites that minimizes the joint uncertainty in spatial and momentum coordinates. The parameter σ defines the spatial spread of the coherent state and defines the uncertainties in space and momentum according to the well-known relation

$$\Delta x \propto \frac{1}{\Delta k} \propto \sigma. \tag{1}$$

As a result, there is a tradeoff for any value of σ selected: for small σ, there is better spatial resolution but poorer resolution in k space, and vice versa for large σ.

Writing out the dot product of the wave function and the coherent state

$$\langle\psi|\mathbf{r}_0,\mathbf{k}_0,\sigma\rangle = \left(\frac{1}{\sigma\sqrt{\pi/2}}\right)\sum_i \psi(\mathbf{r}_i)e^{-(\mathbf{r}_i-\mathbf{r}_0)^2/4\sigma^2+i\mathbf{k}_0\cdot\mathbf{r}_i}, \tag{2}$$

the Husimi function is defined as

$$\text{Hu}(\mathbf{r}_0,\mathbf{k}_0,\sigma;\psi(\{\mathbf{r}_i\})) = |\langle\psi|\mathbf{r}_0,\mathbf{k}_0,\sigma\rangle|^2. \tag{3}$$

Weighting the Husimi function by the wave vector $\mathbf{k}_0$ produces the k-space Husimi vector, and weighting it by the group velocity vector $\nabla_{\mathbf{k}}E(\mathbf{k}')$ produces the group-velocity Husimi vector. The latter is a stronger reflection of classical dynamics in the system, and is used for all results in this paper. At each point in the system, we can sweep through k space by rotating the wave vector $\mathbf{k}_0$ along the Fermi surface in the dispersion relation. The multiple Husimi vectors, which result from the full Husimi projection, provide a snapshot of the local momentum distribution. This paper uses 32 wave vectors along the Fermi surface of two-dimensional graphene to produce group-velocity Husimi projections.[25]

Even though a few plane waves may dominate the wave function, momentum uncertainty of the coherent state can result in many nonvanishing Husimi vectors. Assuming that the dominant plane waves at a point are sufficiently separated in k space, it is possible to recover their wave vectors using the multimodal algorithm in Mason *et al.*,[25] processing the result to produce a semiclassical map showing the dominant classical paths contributing to a given wave function. This

processed Husimi method singles out the important wave vectors contributing to a wave function at each point.[23]

The integral over Husimi vectors at a single point defines a new vector-valued function $\mathbf{Hu}(\mathbf{r}_0, \sigma; \psi(\{\mathbf{r}\}))$, which is equal to

$$\mathbf{Hu}(\mathbf{r}_0, \sigma; \psi(\{\mathbf{r}_i\})) = \int |\langle\psi|\mathbf{r}_0, \mathbf{k}_0, \sigma\rangle|^2 \mathbf{k}_0 d^d k_0. \quad (4)$$

It has been shown that for $\sigma k \ll 1$, this function is equal to the flux operator.[23] To better represent the classical dynamics of the system we can instead weight the integrand by the group velocity $\nabla_\mathbf{k} E(\mathbf{k}')$ to obtain the group-velocity Husimi flux $\mathbf{Hu}_g[\mathbf{r}_0, \sigma; \psi(\mathbf{r})]$ equal to

$$\mathbf{Hu}_g(\mathbf{r}_0, \sigma; \psi(\{\mathbf{r}_i\})) = \int |\langle\psi|\mathbf{r}_0, \mathbf{k}_0, \sigma\rangle|^2 \nabla_\mathbf{k} E(\mathbf{k}_0) d^d k_0, \quad (5)$$

which is used throughout this paper.

Even though the Husimi projection is related to the flux operator, it provides much more information since it can be used on stationary states that exhibit zero flux, and because it can isolate individual bands and valleys in the dispersion relation. The processed Husimi technique uses coherent states to produce maps of the current flow. These maps follow precisely the uncertainty principle, thus the processed Husimi map renders a much better picture of the classical dynamics underlying the wave function than the flux alone.

B. Honeycomb band structure

This paper examines the honeycomb lattice Hamiltonian using the nearest-neighbor tight-binding approximation

$$H = \sum_i \epsilon_i \mathbf{a}_i^\dagger \mathbf{a}_i - t \sum_{\langle ij \rangle} \mathbf{a}_i^\dagger \mathbf{a}_j, \quad (6)$$

where $\mathbf{a}_i^\dagger$ is the creation operator at orbital site i, and we sum over the set of nearest neighbors. To compare against experiment, the hopping integral value is given by $t = 2.7$ eV, while ϵ is set to the value of the Fermi energy.[1,9] Eigenstates of closed stadium billiard systems are computed using sparse matrix eigensolvers to produce individual wave functions.

We study finite graphene systems extracted from an infinite honeycomb lattice. A filter is applied to remove atom sites, which are attached to only one other atom site, and to bridge undercoordinated sites whose π orbitals would strongly overlap. As a result, each edge is either a pure zigzag, armchair, or mixed boundary, as shown in Fig. 1. Recent studies have suggested that under certain circumstances, zigzag edges reconstruct to form a 5–7 chain,[31] however their scattering properties appear to be identical to regular zigzag boundaries.[32] We have elected not to incorporate these features and leave them to future work.

The band structure for graphene prominently features the two inequivalent K' and K valleys in the energy range of $-t \leqslant E \leqslant t$,[9] as can be seen in Fig. 2. At energies close to the Dirac point $E = 0$, these valleys exhibit a linear dispersion relation and the electron behaves as a four-component spinor Dirac particle (two pseudospins, and two traditional spins). Using the creation operators $\mathbf{a}^\dagger$ and $\mathbf{b}^\dagger$ on the A and B sublattices, respectively (see Fig. 1), the two pseudospinors can be
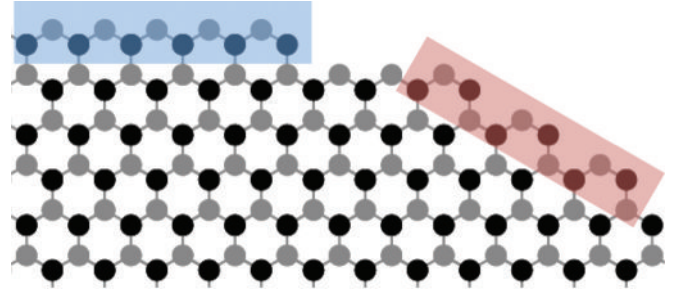

FIG. 1. (Color online) A magnified view of a boundary on a graphene flake. The orientation of the cut relative to the orientation of the lattice can produce two edge types, zigzag (highlighted in blue) and armchair (highlighted in red). The two sublattices of the unit cell are indicated in black (A sublattice) and gray (B sublattice).

written as

$$\psi_{\pm, \mathbf{K}}(\mathbf{k}) = \frac{1}{\sqrt{2}}(e^{-i\theta_\mathbf{k}/2}\mathbf{a}^\dagger \pm e^{i\theta_\mathbf{k}/2}\mathbf{b}^\dagger) \quad (7)$$

$$\psi_{\pm, \mathbf{K}'}(\mathbf{k}) = \frac{1}{\sqrt{2}}(e^{i\theta_\mathbf{k}/2}\mathbf{a}^\dagger \pm e^{-i\theta_\mathbf{k}/2}\mathbf{b}^\dagger), \quad (8)$$

where $\theta_\mathbf{k} = \arctan(\frac{q_x}{q_y})$, $\mathbf{q} = \mathbf{k} - \mathbf{K}^{(\prime)}$ and the $\pm$ signs indicate whether the positive- or negative-energy solutions are being used.[9] While the linear dispersion no longer applies at energies above $\sim 0.4t$, the Dirac basis remains useful as a means of describing the classical dynamics of graphene throughout the energy range $-t \leqslant E \leqslant t$. States near the Dirac point and at the upper edge of this spectrum are examined in this paper.

It might be tempting to obtain a representation of either valley in a graphene wave function by subtracting off a plane wave whose wave vector corresponds to the origin of either K or K' valley, leaving behind the residual $\mathbf{q} = \mathbf{k} - \mathbf{K}^{(\prime)}$. However, this approach only works when quasiparticles are present in only one valley, an assumption that cannot be generally guaranteed.
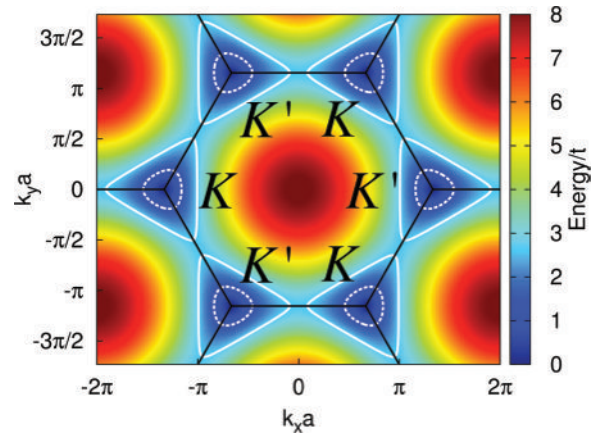

FIG. 2. (Color online) The two-dimensional dispersion relation for graphene demonstrates the two inequivalent valleys as cones where the edges of the Brillouin zones (black lines) meet. Dashed white lines indicate the one-dimensional dispersion surface at $E = 0.5t$, while solid white lines indicate $E = 0.98t$, demonstrating extreme trigonal warping.

On the other hand, since wave vectors for each valley are sufficiently separated in k space, the Husimi projection can distinguish each valley unambiguously for most momentum uncertainties. Because the valleys are part of the same band, a scattered quasiparticle from one valley can emerge in the other.[33] When this occurs, the processed Husimi map shows quasiparticles in one valley funneling into a drain, and quasiparticles in the other valley emitting from a source at the same point, leaving behind a signature for intervalley scattering.

Between $-t < E < t$, the Fermi energy contours warp from a circular shape near the Dirac point to trigonal contours, which emphasize three directions for each valley in the distribution of group velocities $v_g = \Delta_{\mathbf{k}} E(\mathbf{k})$. As a result, the magnitude of the wave vector $\mathbf{q} = \mathbf{k} - \mathbf{K}^{(\prime)}$ depends on its orientation: It is bounded above by

$$q_{\mathrm{up}} = \frac{2}{a} \cos^{-1}\left[\frac{E + t + \sqrt{-3E^2 - 6Et + 9t^2}}{4t}\right], \quad (9)$$

and from below by

$$q_{\mathrm{low}} = \frac{2}{a} \cos^{-1}\left[\frac{-E + t + \sqrt{-3E^2 + 6Et + 9t^2}}{4t}\right]. \quad (10)$$

When characterizing the momentum uncertainty, we use the average of these two quantities.

III. RESULTS

A. States away from the Dirac point

Figure 3 shows processed Husimi maps for three eigenstates of a large closed-system stadium billiard with 20 270 orbital sites for three different energies. We have chosen these states because they exhibit very clear linear trajectories. At energies close to $E = t$, the trajectories exhibit pronounced trigonal warping, as seen by the three preferred directions. While the classical trajectories are obvious in the wave function itself, the processed Husimi map identifies the direction of each trajectory with respect to each valley.

The presence a few dominant classical paths in each wave function in Fig. 3 allows us to infer the relationship between boundary types and scattering among the two Dirac valleys. When a quasiparticle in one valley scatters into the other, it appears in the processed Husimi map as a drain. We can measure this by summing the divergence for all angles in the map as

$$Q_{\mathrm{div.}}(\mathbf{r}; \Psi) = \int D(\mathbf{r}, \mathbf{k}; \Psi)|\nabla_{\mathbf{k}} E(\mathbf{k})| d^d k', \quad (11)$$

where $D(\mathbf{r}, \mathbf{k}; \Psi)$ is defined as the divergence of the processed Husimi map for one wave vector $\mathbf{k}$,

$$D(\mathbf{r}, \mathbf{k}; \Psi) = \int \sum_{i=1}^{d} \frac{\mathrm{Hu}(\mathbf{k}, \mathbf{r}'; \Psi) - \mathrm{Hu}(\mathbf{k}, \mathbf{r}; \Psi)}{(\mathbf{r}' - \mathbf{r}) \cdot \mathbf{e}_i}$$

$$\times \exp\left[\frac{(\mathbf{r}' - \mathbf{r})^2}{2\sigma^2}\right] d^d r', \quad (12)$$

where we sum over the d orthogonal dimensions each associated with unit vector $\mathbf{e}_i$. The divergence in the K' valley, seen in green and red (for positive and negative values,
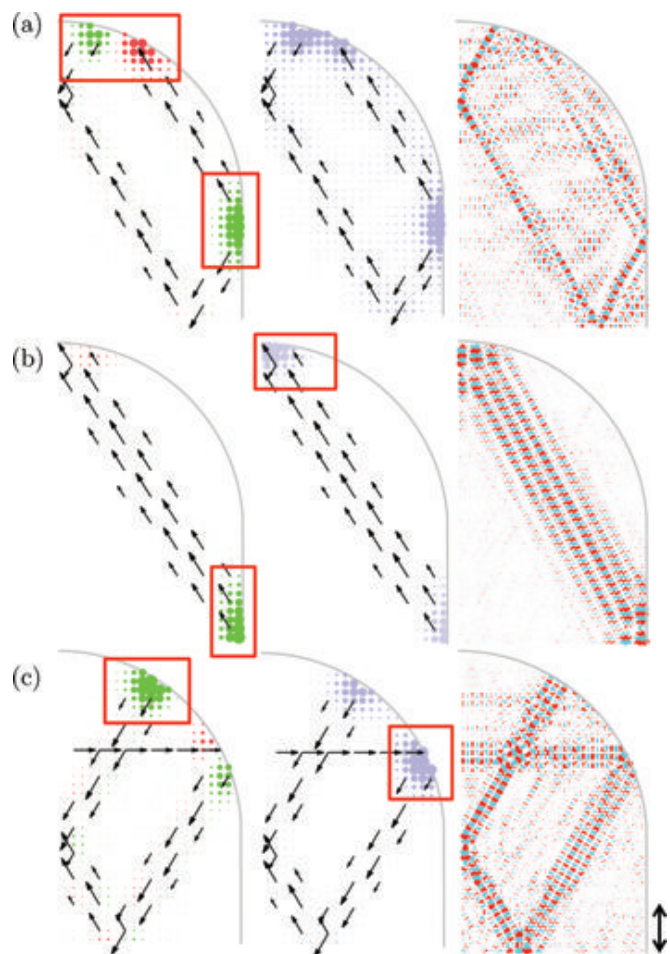

FIG. 3. (Color online) Processed Husimi maps (left and central plots) and eigenstates (right plots) of the closed graphene stadium billiard with 20 270 orbital sites at energies $E = 0.974t$(a), $0.964t$(b), and $0.951t$(c). All three calculations use coherent states with relative uncertainty $\Delta k/k = 30\%$, whose breadth is indicated by the double arrows on the right. Only the upper-right quarter of each stadium is shown. The left plots present the multimodal analysis for the K' valley. The magnitude of the divergence of the processed Husimi map [Eq. (11)] is indicated in green (red) for positive (negative) values. The central panels present the magnitude of the angular deflection indicated in blue [Eq. (13)]. Red boxes indicate scattering regions magnified in Fig. 4.

respectively) in Figs. 3 and 4, shows that the scattering points all lie along nonzigzag boundaries. Plots for the K valley (not shown) are inverted, corroborating the time-reversal symmetry relationship between the two valleys.

On the other hand, when a quasiparticle in one valley reflects off a boundary but does *not* scatter into the other valley, the divergence is zero, but the reflection can still be measured in the angular deflection of the processed Husimi map,

$$Q_{\mathrm{ang.}}(\mathbf{r}; \Psi) = \int |D_{\mathrm{abs.}}(\mathbf{r}, \mathbf{k}; \Psi) \nabla_{\mathbf{k}} E(\mathbf{k})| d^d k. \quad (13)$$

$D_{\mathrm{abs.}}(\mathbf{r}, \mathbf{k}; \Psi)$ is defined as the *absolute* divergence of the Husimi function for one particular trajectory angle with a wave
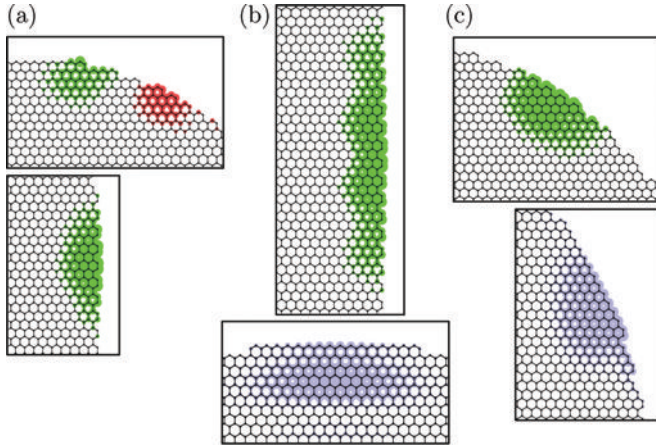
FIG. 4. (Color online) Magnified views of the divergence and angular deflection in Fig. 3 (red boxes). The sources and drains in the K'-valley processed Husimi map are actually intervalley scattering points, which occur along nonzigzag boundaries. In contrast, points of angular deflection that are *not* sources or drains correspond to *intravalley* scatterers and occur along pure or nearly pure zigzag boundaries.

vector $\mathbf{k}$,

$$D_{\text{abs.}}(\mathbf{r},\mathbf{k};\Psi) = \int \sum_{i=1}^{d} \left| \frac{\text{Hu}(\mathbf{k},\mathbf{r}';\Psi) - \text{Hu}(\mathbf{k},\mathbf{r};\Psi)}{(\mathbf{r}' - \mathbf{r}) \cdot \mathbf{e}_i} \right|$$

$$\times \exp\left[\frac{(\mathbf{r}' - \mathbf{r})^2}{2\sigma^2} \right] d^d r'. \tag{14}$$

As a result, boundary points with large angular deflection are either intervalley or intravalley scatterers depending on the magnitude of divergence at each point.

In Figs. 3 and 4, we plot the angular deflection in blue to compare to the divergence in green and red. Using this information, we can determine that for the wave function in Fig. 3(a), all boundary scattering points are intervalley scatterers, since all points of angular deflection exhibit divergence. The wave function in Fig. 3(b), on the other hand, only exhibits divergence along the vertical sides of the stadium billiard: the horizontal top edge exhibits strong angular deflection but *no* divergence, and constitutes an intravalley scatterer. Examining the magnified views in Figs. 4(a) and 4(b), we see that intervalley scatterers correspond to armchair edges and the intravalley scatterers belong to zigzag edges, corroborating the findings at the Dirac point by Akhmerov and Beenakker.[34] Similar points of scattering can also be found in Figs. 3(c) and 4(c).

Because of the time-reversal relationship between the two valleys, the severe restriction on group velocities, and the placement of zigzag and armchair boundaries, no path at these energies exists *without* interacting with an intervalley scatterer (data not shown). By comparison, it is not only possible but common to find states near the Dirac point that exhibit the opposite: all boundary conditions which are expressed belong to only intravalley scatterers (see Sec. III B).

In comparison to Fig. 3, the eigenstate of the much smaller graphene stadium system in Fig. 5 does not appear to show isolated trajectories in its wave function representation. This is not surprising since this system can only accommodate
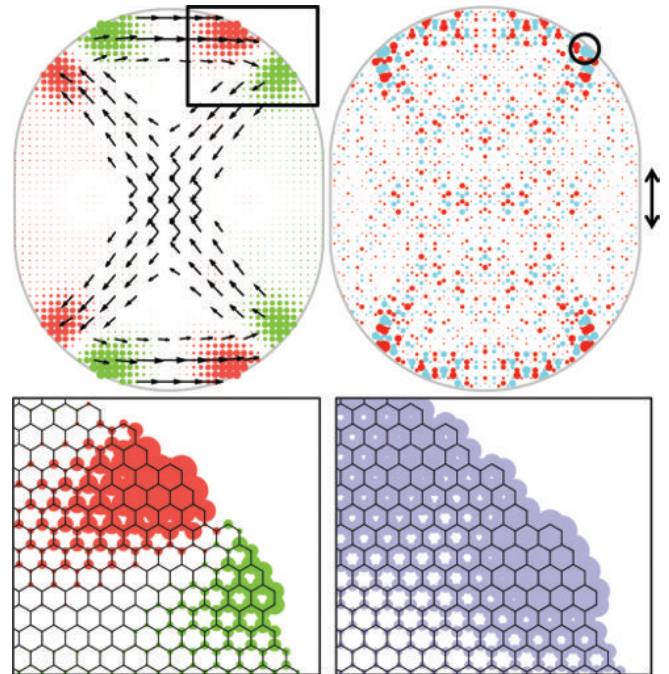
FIG. 5. (Color online) A closed-system eigenstate at $E = 0.72t$ for the smaller graphene stadium. At top, the filtered multimodal analysis with relative momentum uncertainty $\Delta k/k = 30\%$ along with the wave function (right). The spread of the coherent state is indicated by the double arrows. Bottom, higher-resolution calculations of the divergence (green for positive, red for negative) and the angular deflection (blue) are shown against the graphene structure. The black circle indicates where the system boundary is perturbed in the original paper[27] as discussed in Sec. III C.

five de Broglie wavelengths vertically, and three horizontally, severely restricting its ability to resolve such trajectories. However, clear self-retracing trajectories are quite visible in the processed Husimi map in Fig. 5, with evident sources and drains inhabiting the boundary, showing that the processed Husimi flow can yield a semiclassical interpretation of the dynamics of the states not possible from just the wave function of the system. Moreover, because the paths indicated by the map marshal the electron away from lateral boundaries, where leads connect to produce the open system in Sec. III C, the processed Husimi map helps us understand the role this state plays in forming a long-lived resonance in the open system.

In both Figs. 3 and 5, wave functions in graphene away from the Dirac point are linked to valley switching classical ray paths, which bounce back and forth along straight lines. These wave function enhancements are not strictly scars,[26] as first suggested by Huang *et al.*,[27] since scars are generated by unstable classical periodic orbits in the analogous classical limit (group velocity) system. Instead, the wave-function structures are more likely normal quantum confinement to stable zones in classical phase space constrained by group-velocity warping at these energies.

B. States near the Dirac point

We now explore the properties of low-energy closed-system states in graphene, using the circular graphene flake and
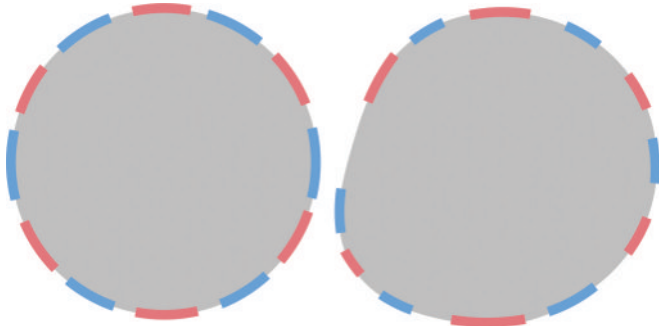
FIG. 6. (Color online) Schematic indicating the locations of armchair (blue) and zigzag (red) edges in the circular system (left) and the Wimmer system (right).

the distorted circular flake introduced by Wimmer *et al.*[35] The latter geometry was chosen because its dynamics are chaotic and sensitive to the placement of armchair and zigzag boundaries, which shift as a result of the distortion. We indicate the two boundary types for both geometries in Fig. 6.

In the continuous system, the Fermi wave vector grows with the square root of the energy, but in graphene, the effective wave vector $\mathbf{q} = \mathbf{k} - \mathbf{K}^{(\prime)}$ grows linearly. As a result, the de Broglie wavelength is much larger for the graphene system than for the continuous system at similar energy scales, making it difficult to conduct calculations with sufficient structure in the wave function. Consequently, we examine states at energies away from the Dirac point to bring calculations within a reasonable scope. (For instance, we have selected a system size under 100 000 orbital sites to facilitate replication of our results). Since trigonal warping becomes significant above $E = 0.4t$, we have selected the energy of $0.2t$ for all states in our analysis to maximize the number of wavelengths within a small graphene system while maintaining the same physics from energies closer to the Dirac point.

Figure 7 shows four eigenstates of the circular graphene flake. Like the free-particle circular well, eigenstates of the graphene circular flake resemble eigenstates of the angular momentum operator (see Mason *et al.*[23,24] for direct comparisons and processed Husimi maps). For instance, the wave functions in Figs. 7(a) and 7(b) are radial dominant, while the wave function in Fig. 7(d) is angular dominant. These observations carry over to the dynamics of the wave functions revealed by the multimodal analysis for the K' valley, which shows radially oriented paths in Figs. 7(a) and 7(b) and circular paths skimming the boundary in Fig. 7(d). Figure 7(c) shows a state with a mixture of radial and angular components; in the multimodal analysis, this appears as straight paths between boundary points highlighted by the angular deflection.

Unlike free-particle circular wells, however, the lattice sampling on the honeycomb lattice breaks circular symmetry and replaces it with sixfold symmetry. Because eigenstates of the system emphasize certain boundary conditions, the manner in which each state establishes itself strongly varies. For instance, the two radial-dominant states in Figs. 7(a) and 7(b) exhibit intravalley (a) or intervalley (b) scattering. Accordingly, the locations where the rays terminate on the boundary correlate with zigzag and armchair boundaries respectively. The wider spread in angular deflection in Fig. 7(a)
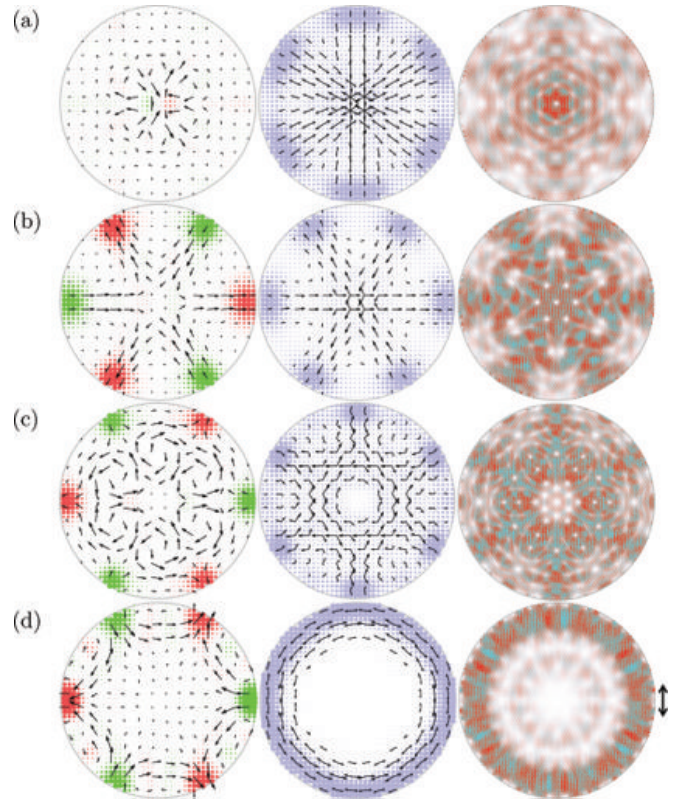

FIG. 7. (Color online) Low-energy graphene states require additional tools to fully grasp the classical dynamics. The processed Husimi map for the K' valley is plotted for four eigenstates of a closed circular system with 71 934 orbital sites at energies around $E = 0.2t$. All three calculations use coherent states with relative uncertainty $\Delta k / k = 20\%$, with breadth indicated by the double arrows on the right. From left to right: the Husimi flux, multimodal analysis, and the wave function. The divergence of the Husimi flux is indicated in green (red) for positive (negative) values. In blue, the angular deflection.

corroborates the findings of Akhmerov and Beenakker,[34] showing that intravalley scattering occurs over a larger set of boundaries than intervalley scattering.

Because each valley reflects back to itself in Fig. 7(a), there is no net flow of either valley in the bulk of the system. As a result, the multimodal analysis shows counterpropagating flows, and the Husimi flux [Eq. (5)] is zero except at the center, where slight offsets in trajectories form characteristic vortices. In Fig. 7(b), on the other hand, each ray in the wave function is associated with a distinct source and drain, which is evident in both the multimodal analysis and the Husimi flux.

In Figs. 7(c) and 7(d), the locations of sources and drains for the K' valley are reversed from Fig. 7(b). However, the roles that intervalley scattering play in these states is less clear; rather, inter- *and* intravalley scattering dominate these wave functions. In Fig. 7(c), this can be seen by the emphasis of angular deflection along the zigzag boundaries, which do not show any divergence. In Fig. 7(d), even though the wave function and the multimodal analysis clearly emphasize a classical path that skims the boundary, the path actually flips between each valley each time it encounters an intervalley scatterer. For both states, the various trajectories merge to form vortices in the Husimi flux, with sources and drains at armchair edges.
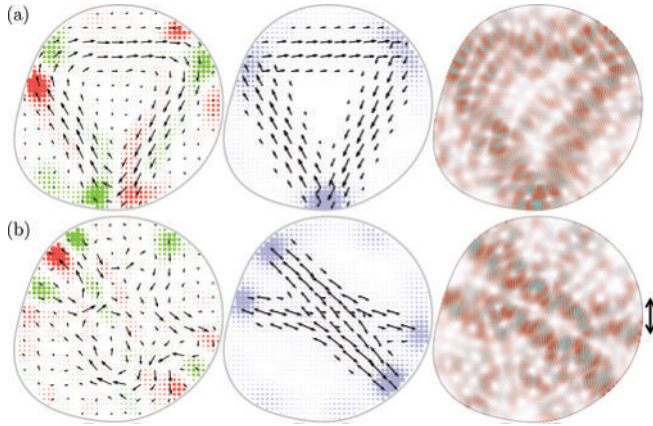
FIG. 8. (Color online) In parts (a) and (b), the same information is plotted as in Fig. 7, but for the Wimmer system (see Fig. 6), with 96 425 orbital sites. These states also have energies near $E = 0.2t$ and are represented by coherent states of uncertainty $\Delta k/k = 20\%$ with breadth indicated by the double arrows.

When the circular flake is distorted, as in the Wimmer system (Figs. 6 and 8), intervalley and intravalley scatterers are rearranged and resized as a function of the local radius of curvature of the boundary.

Figures 8(a) and 8(b) show two eigenstates of the distorted circular flake system. The boundary conditions for these states most closely resemble Fig. 5, since sources and drains appear next to each other. This is a signature of mixed scattering— both intervalley and intravalley scattering occur in various proportions at these points. For example, the multimodal analysis in Fig. 8(a) shows a triangular path, but not all legs of the triangle are equally strong, corresponding to various degrees of absorption and reflection at each scattering point which can be seen in the divergence.

Edge states are a set of zero-energy surface states that are strongly localized to zigzag boundaries and potentially long lived.[9] Since they can be used as modes of transport[10,12] and be strongly spin polarized,[11,13] they have been proposed a candidate for spintronics devices.[9–13] However, because edge states exhibit a different dispersion relation than the two valleys in the bulk, they cannot be sensed by the K'- or K-valley Husimi projections. Instead, the processed Husimi map can be generated using wave vectors appropriate to the edge states, which shows them as standing waves on the surface (see Fig. 9). As noted by Wimmer *et al.*,[35] it is possible for edge states to tunnel into each other using bulk states as a medium, but we have found that K'- or K-valley processed Husimi maps of bulk states, which hybridize with them are indistinguishable from their nonhybridized counterparts

C. Fano resonance

This section addresses Fano resonance[28] in graphene systems, a conductance phenomenon that occurs as a result of interference between a direct state (conductance channel) and a quasibound indirect state similar to the eigenstates this paper has examined. Fano resonances are an ideal case study for the processed Husimi map, not only because they are ubiquitous in theory[36,37] and experiments,[38–40] but also because their behavior is well understood.[30,41–46] However, Fano resonances
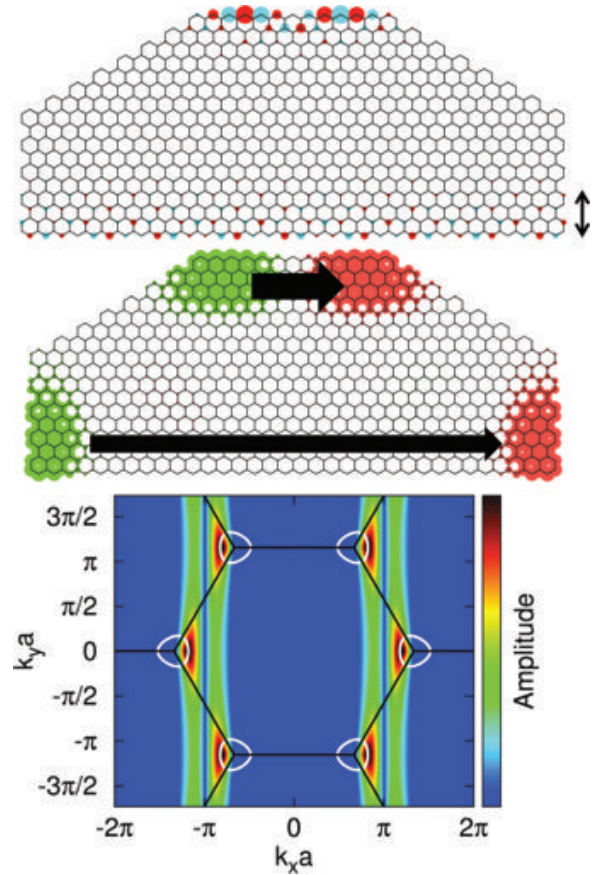

FIG. 9. (Color online) An extremely small rooftop graphene flake at energy $E = 0.0015735t$ showing two edge states at the top and bottom boundaries, which tunnel into each other. At top, the full wave function, at middle, divergence is indicated in green and red, and a schematic of the Husimi flux for the K' valley is shown. At bottom, the Fourier transform of the state is shown with the contour line used to generate the processed Husimi map in white, set at an arbitrary energy in order to maximize the intersection of the contour with the Fourier-transform amplitude. The double arrows indicate the spread of the wave packet used to generate this map.

in *graphene* quantum dots are less well characterized[47–50] and lack a comprehensive theory relating boundary conditions to bulk state behavior in graphene.

To study Fano resonance, we first compute a scattering wave function using the recursive numerical Green's function method.[51] The advantage this method presents is that we can obtain a scattering density matrix ρ, which is then diagonalized. Each eigenvector corresponds to a scattering wave function, which has an associated eigenvalue indicating its measurement probability (Fig. 10, middle). We focus on the resonance studied by Huang *et al.*[27]

The resonance in Fig. 10 is associated with the eigenstate from Fig. 5 of the closed billiard system. This eigenstate couples only weakly to leads, which are attached at its sides (shown in the inset of Fig. 10). This makes it possible for a scattering electron to enter the system through a direct channel but then become trapped in a quasibound state related to the eigenstate, causing the density of states projected onto the eigenstate to strongly peak near its eigenenergy (Fig. 10,
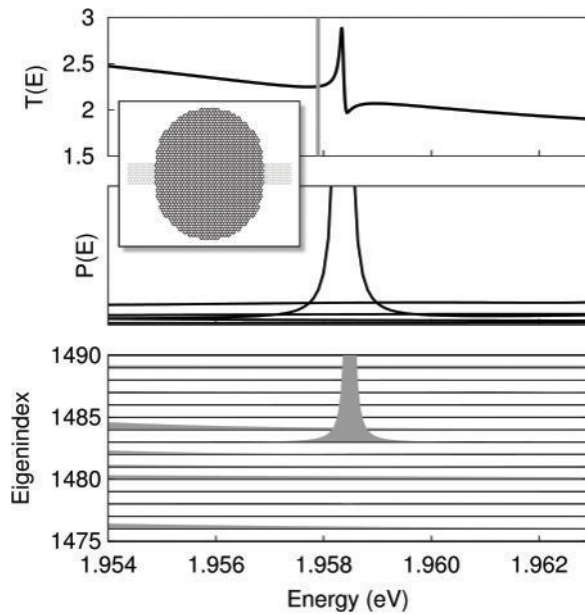
FIG. 10. System properties of the scattering density matrix ρ around the Fano resonance centered at $E = 1.9582$ eV for the open system in the inset. Top: The transmission profile across the two leads, with the closed-system eigenstate energy at $E = 1.9579$ eV, corresponding to the eigenstate at index 1483 (below), indicated by the vertical gray line. Middle: Diagonalizing the density matrix produces a handful of nontrivial scattering wave functions in its eigenvectors. The eigenvalues of these vectors, which correspond to their measurement probability, are graphed. The wave function associated with the closed-system eigenstate hybridizing with the direct channel peaks strongly around the Fano resonance. Bottom: The density matrix is projected onto the closed-system eigenstates, showing that eigenstate 1483 strongly peaks at the Fano resonance.

bottom). As the system energy sweeps across the eigenenergy, the phase of the eigenstate component shifts through π, causing it to interfere negatively and then positively with the direct channel, giving rise to the distinctive Fano curve (Fig. 10, top). As a result, the scattering wave function with the largest measurement probability is in fact a hybridized state between the closed-system eigenstate and the direct channel, and its probability peaks around an energy near, but not exactly the same as, the eigenstate energy (Fig. 10, middle). The shift in energy arises as a perturbation from the leads.

For closed graphene systems, the two valleys satisfy time-reversal symmetry as an analytical consequence of lattice sampling on the honeycomb lattice. As a result, trajectories in one valley are exactly reversed from the other valley, in analogy with free-particle systems where opposing trajectories cancel each other produce zero flux. This observation allows us to remove the time-reversal symmetry of a scattering wave function by summing the projections for both valleys, revealing the time-reversal *asymmetric* part of the wave function.

Figure 11 shows the results of adding the Husimi flux maps of both valleys at two energies, below and above resonance. We find sources and drains in the summed Husimi flux map at the corners of the system where the classical paths of the K'-valley processed Husimi map (Fig. 5) reflect off the system boundary.
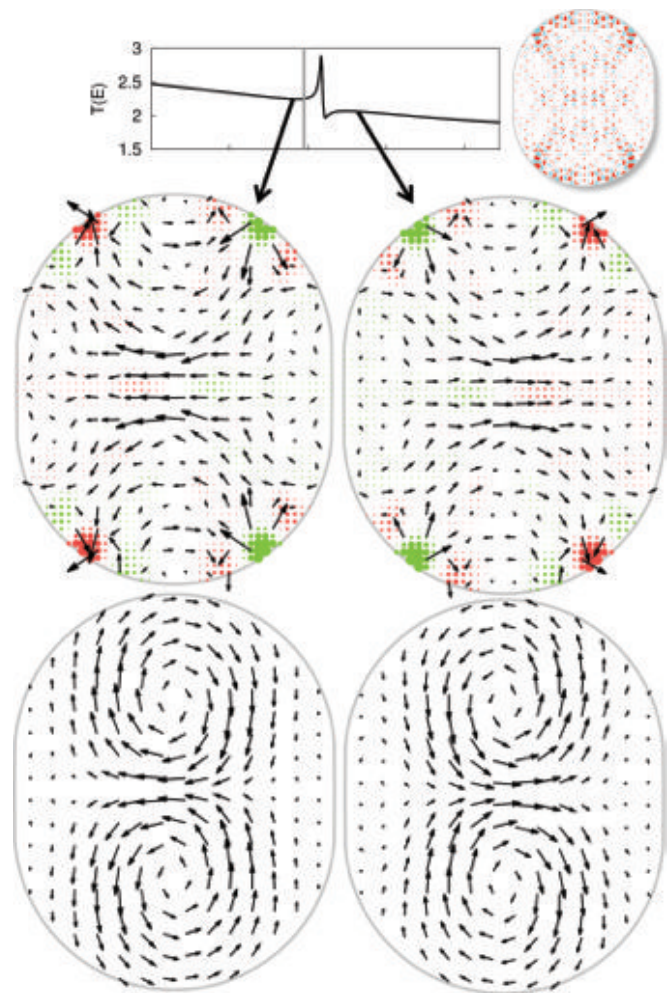

FIG. 11. (Color online) Above and below the Fano resonance in Figs. 10 (inset), the time-reversal symmetry between the K and K' valleys is lifted, making it possible to add the Husimi flux for both valleys to measure valley-polarized current. Above, the Husimi flux maps of both valleys are added for the scattering wave function at energies $E = 1.9582t$ and $1.9586t$, with $\Delta k/k = 30\%$. Below, the probability flux, convolved with a Gaussian kernel of the same size as the coherent state. At energies this close to resonance, the wave function does not visually change from the closed-system eigenstate in the inset, but the residual current that occurs near these resonances switches direction across resonance.

To understand why, we consider that during transmission, quasiparticles enter from the left incoming lead and exit through the right outgoing lead. However, near resonance, the wave function is strongly weighted by the closed-system eigenstate, which has *no* net quasiparticle current. Processed Husimi maps for either valley also reflect this fact: they are indistinguishable from the maps of the closed-system eigenstate in Fig. 5, and the two valleys are inverse images of each other.

However, the processed Husimi maps for the two valleys don't exactly cancel each other out. When we add them together to reveal the time-reversal asymmetric behavior of the wave function, the residual shows sources and drains of net quasiparticle flow, which are strongly related to the maps for each valley, and do *not* show left-to-right transmission.

Instead, the summed Husimi flux map shows the influence of transmission on the strongly emphasized classical paths underlying the closed-system eigenstate.

To compare the summed Husimi flux map to the traditional flux, we consider the probability flow between two adjacent carbon atom sites called the bond current, defined as

$$j_{i \to j} = \frac{4e}{h} \text{Im}\big[H_{ij} G_{ij}^n(E) \big], \tag{15}$$

where H_{ij} and $G_{ij}^n(E)$ are the off-diagonal components of the Hamiltonian and the electron correlation function between orbital sites i and j.[41,52] The electron correlation function is proportional to the density matrix, but in our calculations, we examine just one scattering state, so that $G_{ij}^n \propto \psi_i \psi_j^*$ where ψ_i is the scattering state probability amplitude at orbital site i. We can obtain a finite-difference analog of the continuum flux operator by defining

$$\mathbf{j}_i = \sum_j j_{i \to j} \frac{\mathbf{r}_j - \mathbf{r}_i}{|\mathbf{r}_j - \mathbf{r}_i|^2}, \tag{16}$$

which computes the vector sum of each bond current associated with a given orbital.[53]

Convolving the flux defined in Eq. (16) with a Gaussian kernel of the same spread as the coherent state used to generate the processed Husimi map creates an analog to the Husimi flux, except that the convolved flux does not distinguish among valleys. We present the convolved flux at the bottom of Fig. 11, and find that it forms vortices, which correlates with the summed Husimi flux maps, while not showing the left-to-right flow responsible for transmission.

This behavior is directly analogous to flux in continuum systems, where flux vortices above and below resonance show local variations of flow but not the left-to-right drift velocity responsible for transmission. We can recover the left-to-right flow only by examining the system at larger scales using larger Gaussian spreads (not shown).[24] Because of the π phase shift of the indirect channel across resonance, local flows reverse direction above and below resonance, but they do not affect the left-to-right flow at larger scales except exactly on resonance.

The stable orbits that underly the indirect channel, shown in Fig. 5, can be dramatically disturbed by slight modifications of the boundary where the classical paths reflect off the boundary. Huang *et al.*[27] examined the relationship between system symmetry and strength of the Fano resonances by slightly modifying the system boundary at the black circle in Fig. 5, and demonstrated that some resonances were drastically reduced by this modification. We have chosen the resonance in this study because the Fano resonance profile associated with it was among the most reduced as a result of their system modification, and our analysis provides a clear picture as to why: the system is perturbed precisely at the boundary where the eigenstate in Fig. 5 has the largest probability amplitude.

The semiclassical analysis adds an intuitive understanding: by disturbing the reflection angle at the exact point where the two valleys scatter, each time an electron scatters off that point some of its probability leaves the stable orbit. The perturbation to the boundary effectively introduced a leak into the orbit, reducing its lifetime and the strength of the associated resonance considerably.

IV. CONCLUSIONS

We have examined the semiclassical behavior of graphene systems using a generalized technique that produces a vector field from projections onto coherent states, forming an infinitely tunable bridge between the large-scale Dirac effective field theory and the underlying atomistic model.[9] We have used this technique, called the processed Husimi map, to examine the relationship between graphene boundary types and the classical dynamics of quasiparticles in each valley of the honeycomb dispersion relation, studying states with energies both close to and far from the Dirac point. We have shown that closed-system eigenstates are associated with valley-polarized currents with zero net quasiparticle production. We have shown that Fano resonances are associated with an asymmetrical flow of quasiparticles strongly related to the valley-polarized currents of closed-system states, which has implications for applications in valleytronic devices.[54] The ubiquity of this phenomenon in the systems we have studied suggests that they could appear in future experiments, and provides a motivation for further theoretical and experimental work.

[1] A. K. Geim and K. S. Novoselov, Nat. Mater. **6**, 183 (2007).

[2] M. Y. Han, B. Özyilmaz, Y. Zhang, and P. Kim, Phys. Rev. Lett. **98**, 206805 (2007).

[3] K. S. Novoselov, Z. Jiang, Y. Zhang, S. V. Morozov, H. L. Stormer, U. Zeitler, J. C. Maan, G. S. Boebinger, P. Kim, and A. K. Geim, Science **315**, 5817 (2007).

[4] E. Stolyarova, K. T. Rim, S. Ryu, J. Maultzsch, P. Kim, L. E. Brus, T. F. Heinz, M. S. Hybertsen, and G. W. Flynn, Proc. Natl. Acad. Sci. USA **104**, 9209 (2007).

[5] G. M. Rutter, J. N. Crain, N. P. Guisinger, T. Li, P. N. First, and J. A. Stroscio, Science **317**, 219 (2007).

[6] Y. Zhang, V. W. Brar, C. Girit, A. Zettl, and M. F. Crommie, Nat. Phys. **5**, 722 (2009).

[7] J. Berezovsky, M. F. Borunda, E. J. Heller, and R. M. Westervelt, Nanotechnology **21**, 274013 (2010).

[8] J. Berezovsky and R. M. Westervelt, Nanotechnology **21**, 274014 (2010).

[9] A. H. Castro Neto, F. Guinea, N. M. R. Peres, K. S. Novoselov, and A. K. Geim, Rev. Mod. Phys. **81**, 109 (2009).

[10] M. Wimmer, I. Adagideli, S. Berber, D. Tománek, and K. Richter, Phys. Rev. Lett. **100**, 177207 (2008).

[11] W. L. Wang, S. Meng, and E. Kaxiras, Nano Lett. **8**, 241 (2008).

[12] M. Wimmer, M. Scheid, and K. Richter, in *Encyclopedia of Complexity and Systems Science*, edited by R. A. Meyers (Springer, New York, 2009), pp. 8597–8616.

[13] W. L. Wang, O. V. Yazyev, S. Meng, and E. Kaxiras, Phys. Rev. Lett. **102**, 157201 (2009).

[14] T. O. Wehling, K. S. Novoselov, S. V. Morozov, E. E. Vdovin, M. I. Katsnelson, A. K. Geim, and A. I. Lichtenstein, Nano Lett. **8**, 173 (2008).

[15] S. Schnez, J. Güttinger, M. Huefner, C. Stampfer, K. Ensslin, and T. Ihn, Phys. Rev. B **82**, 165445 (2010).

[16] T. O. Wehling, A. V. Balatsky, M. I. Katsnelson, A. I. Lichtenstein, K. Scharnberg, and R. Wiesendanger, Phys. Rev. B **75**, 125425 (2007).

[17] L. Simon, C. Bena, F. Vonau, D. Aubel, H. Nasrallah, M. Habar, and J. C. Peruchetti, Eur. Phys. J. B **69**, 351 (2009).

[18] H. Amara, S. Latil, V. Meunier, Ph. Lambin, and J.-C. Charlier, Phys. Rev. B **76**, 115423 (2007).

[19] M. I. Katsnelson and A. K. Geim, Phil. Trans. R. Soc. A **366**, 195 (2008).

[20] P. Koskinen, S. Malola, and H. Häkkinen, Phys. Rev. B **80**, 073401 (2009).

[21] J. Tian, H. Cao, W. Wu, Q. Yu, and Y. P. Chen, Nano Lett. **11**, 3663 (2011).

[22] K. A. Ritter and J. W. Lyding, Nat. Mater. **8**, 235 (2009).

[23] D. J. Mason, M. F. Borunda, and E. J. Heller, Europhys. Lett. **102**, 60005 (2013).

[24] D. J. Mason, M. F. Borunda, and E. J. Heller, arXiv:1205.3708.

[25] D. J. Mason, M. F. Borunda, and E. J. Heller, arXiv:1206.1013.

[26] E. J. Heller, Phys. Rev. Lett. **53**, 1515 (1984).

[27] L. Huang, Y.-C. Lai, D. K. Ferry, S. M. Goodnick, and R. Akis, Phys. Rev. Lett. **103**, 054101 (2009).

[28] U. Fano, Phys. Rev. **124**, 1866 (1961).

[29] D. K. Ferry, J. P. Bird, R. Akis, D. P. Pivin Jr., K. M. Connolly, K. Ishibashi, Y. Aoyagi, T. Sugano, and Y. Ochiai, Jpn. J. Appl. Phys. **36**, 3944 (1997).

[30] A. E. Miroshnichenko, S. Flach, and Y. S. Kivshar, Rev. Mod. Phys. **82**, 2257 (2010).

[31] P. Koskinen, S. Malola, and H. Häkkinen, Phys. Rev. Lett. **101**, 115502 (2008).

[32] J. A. M. van Ostaay, A. R. Akhmerov, C. W. J. Beenakker, and M. Wimmer, Phys. Rev. B **84**, 195434 (2011).

[33] N. W. Ashcroft and N. D. Mermin, *Solid State Physics* (Saunders, Philadelphia, 1976).

[34] A. R. Akhmerov and C. W. J. Beenakker, Phys. Rev. B **77**, 085423 (2008).

[35] M. Wimmer, A. R. Akhmerov, and F. Guinea, Phys. Rev. B **82**, 045409 (2010).

[36] D. K. Ferry, R. Akis, and J. P. Bird, Phys. Rev. Lett. **93**, 026803 (2004).

[37] F. Muñoz-Rojas, D. Jacob, J. Fernández-Rossier, and J. Palacios, Phys. Rev. B **74**, 195417 (2006).

[38] J. Göres, D. Goldhaber-Gordon, S. Heemeyer, M. A. Kastner, Hadas Shtrikman, D. Mahalu, and U. Meirav, Phys. Rev. B **62**, 2188 (2000).

[39] K. Kobayashi, H. Aikawa, A. Sano, S. Katsumoto, and Y. Iye, Phys. Rev. B **70**, 035319 (2004).

[40] L. E. Calvet, J. P. Snyder, and W. Wernsdorfer, Phys. Rev. B **83**, 205415 (2011).

[41] S. Datta, *Electronic Transport in Mesoscopic Systems* (Cambridge University Press, Cambridge, 1997).

[42] L. L. Sohn, L. P. Kouwenhoven, and G. Schön, *Mesoscopic Electron Transport* (Kluwer Academic, Dordrecht, 1997).

[43] D. K. Ferry and S. M. Goodnick, *Transport in Nanostructures* (Cambridge University Press, Cambridge, 1999).

[44] K. Igor'O and R. Ellialtioĝlu, *Quantum Mesoscopic Phenomena and Mesoscopic Devices in Microelectronics* (Springer, Berlin, 2000).

[45] J. P. Bird, *Electron Transport in Quantum Dots* (Kluwer Academic, Dordrecht, 2003).

[46] S. Datta, *Quantum Transport: Atom to Transistor* (Cambridge University Press, Cambridge, 2005).

[47] J. Wurm, A. Rycerz, I. Adagideli, M. Wimmer, K. Richter, and H. U. Baranger, Phys. Rev. Lett. **102**, 056806 (2009).

[48] L. Huang, Y.-C. Lai, D. K. Ferry, R. Akis, and S. M. Goodnick, J. Phys.: Condens. Matter **21**, 344203 (2009).

[49] D. K. Ferry, L. Huang, R. Yang, Y.-C. Lai, and R. Akis, J. Phys. Conf. Ser. **220**, 012015 (2010).

[50] L. Huang, R. Yang, and Y.-C. Lai, Europhys. Lett. **94**, 58003 (2011).

[51] D. J. Mason, D. Prendergast, J. B. Neaton, and E. J. Heller, Phys. Rev. B **84**, 155401 (2011).

[52] J.-Y. Yan, P. Zhang, B. Sun, H.-Z. Lu, Z. Wang, S. Duan, and X.-G. Zhao, Phys. Rev. B **79**, 115403 (2009).

[53] L. P. Zârbo and B. K. Nikolić, Europhys. Lett. **80**, 47001 (2007).

[54] A. Rycerz, J. Tworzydlo, and C. W. J. Beenakker, Nat. Phys. **3**, 172 (2007).